



Cobalt single atom anchored on *N*-doped carbon nanoboxes as typical single-atom catalysts (SACs) for boosting the overall water splitting

Tong Li^a, Siyuan Ren^a, Cheng Zhang^a, Lingxia Qiao^a, Jiang Wu^{a,b,*}, Ping He^a, Jia Lin^c, Yongsheng Liu^{c,*}, Zaiguo Fu^a, Qunzhi Zhu^a, Weigu Pan^a, Baofeng Wang^d, Zhongwei Chen^{e,*}

^a College of Energy and Mechanical Engineering, Shanghai University of Electric Power, Shanghai 200090, China

^b Shanghai Non-carbon Energy Conversion and Utilization Institute, Shanghai 200240, China

^c College of Mathematics and Physics, Shanghai University of Electric Power, Shanghai 200090, China

^d College of Environmental and Chemical Engineering, Shanghai University of Electric Power, Shanghai 200090, China

^e Department of Chemical Engineering, Waterloo Institute for Nanotechnology, University of Waterloo, Canada



ARTICLE INFO

Keywords:

Single-atom catalysts
N-doped carbon nanoboxes
 Water splitting

ABSTRACT

Single-atom catalysts (SACs) are considered one of the promising strategies to achieve efficient energy conversion, due to their advantage of both maximum atomic utilization and minimum catalyst cost. However, finding a balance between increasing the atom loading and preventing the agglomeration of metal single atoms is a current research hotspot. Herein, we have developed single-atom cobalt embedded in *N*-doped carbon nanoboxes as high-efficiency bifunctional electrocatalysts for overall water splitting in alkaline/acidic electrolytes. Due to the reliable metal-nonmetal bonds between the Co single atom and the substrate carbon, where the uniformly dispersed Co atoms could be effectively and stably riveted on the carbon nanoboxes, and the as-prepared electrocatalyst possesses high mass loading of single Co atoms (~10.2 wt%). In addition, the systematic X-ray absorption fine structure (XAFS) and density functional theory (DFT) calculations were performed to further investigate the relationship between coordination number, configuration and electrocatalytic properties of Co single atoms and N atoms. Based on the above results, the presence of Co atoms induces the formation of pyrr-N and possesses Co@CNB-N₄ configuration with HER overpotential of 45 mV, comparable to Pt/C (20 wt%). As for OER, Co@CNB-N₄ still has satisfactory catalytic performance, superior to the benchmark catalyst RuO₂. Thus, this work builds a bridge to understand the impact of metal single atoms and substrate configuration on catalytic performance and opens a door to the successful synthesis of SACs with high loading of non-precious metal atoms, high atomic utilization and electrocatalytic activity.

1. Introduction

Along with the rapid expansion of the world economy, plants consume large amounts of fossil fuels and non-environmentally friendly energy, posing an inescapable global climate problem. More and more attention are being focused on seeking and developing new sustainable green energy systems and storage technology strategies [1–6]. Hydrogen is highly regarded as a zero-polluting combustible gas, with only pure water as a combustion product [7–10]. Electrocatalytic overall water splitting is generally considered a potential technological route for the conversion of renewable energy sources into hydrogen via electrical energy and thus achieve energy storage, enabling continuous large-scale storage and industrial use of renewable resources [11–16]. Generally,

two half-reactions, oxygen evolution reaction (OER) and hydrogen evolution reaction (HER), which occur at the anode and cathode, respectively, together consist of the overall water splitting [17–22]. Both of them are non-spontaneous reactions, which require additional energy to overcome the reaction energy barriers of each half-reaction. These processes consume lots of energy, therefore effective electrocatalysts are required to reduce the reaction overpotentials. Typically, Ir/Ru oxides and Pt are widely applied as benchmark electrocatalysts for OER and HER, respectively [23–27]. Unfortunately, the large-scale and sustainability of precious metal-based electrocatalysts are resisted by scarcity, high cost and moderate long-term durability. Among the published research, later transition metal (Fe, Co, Ni, et al.) and carbon-based substrates (carbon nanotubes, carbon nanowires, carbon nanospheres,

* Corresponding authors.

E-mail addresses: wjcf2002@163.com (J. Wu), yliu@shiep.edu.cn (Y. Liu), zhwchen@uwaterloo.ca (Z. Chen).

et al.) composite catalysts have been widely reported and intensively explored, due to the excellent catalytic potential of later transition metals, the good electrical conductivity of carbon-based substrates and flexible and versatile coupling routes. However, the irreversible sharp agglomeration and violent deformation of such nanoparticles cause the atomic utilization efficiency of composite materials to remain still very low [28–31]. In this context, to successfully synthesize heterogeneous electrocatalysts, nanoparticles must be downsized to nanodots or even single atoms.

Single-atom catalysts (SACs) have caught the worldwide eye in many fields of catalysis, especially in electrocatalysis. Due to isolated metal atoms anchored on a substrate with different coordination environments, which acts as the catalysis centre, SACs possess outstanding catalytic activity, selectivity and maximum utility of atoms [32–42]. Moreover, SACs blur the line between homogeneous and heterogeneous, creatively modifying substrates to enhance their physical characteristics [43–46]. Specifically, materials with a single metal atom anchored on a carbon substrate which is functionalized by non-metallic elements (N, P, S, et al.) have wide potential in the field of catalysis. Among the cases, the N atom could form stable bonds with a single metal atom and optimize the conformation of the active site at the same time. More importantly, the electronic environment of the central metal single atom can be purposefully influenced by the introduction of different non-metallic atoms, thus achieving the goal of increasing the electrocatalytic activity [47–48]. For instance, Wang et al. [49] synthesized a series of N, S co-doped transition metal-based single-atom electrocatalysts, and the results showed that the catalysts with Fe as the active site exhibited the most excellent ORR electrocatalytic performance attributed to the differences in bond types and structures of different transition metals with N, S atoms. Feng et al. [50] designed a CoN_x/C electrocatalyst prepared by pyrolysis and confirmed that the Co site is the true active centre. Song et al. [51] synthesized $\text{NiFe-g-C}_3\text{N}_4/\text{CNT}$ by high-temperature polymerization and attributed the efficient OER catalytic performance to the high atomic utilization and unique electrocatalytic potential of Ni and Fe bimetal. Even though the above achievements are encouraging, there are still two assignable difficulties that have not yet been solved: 1) Excessive metal atom loading most likely leads to agglomeration of metal single atoms, which results in the very low level of atom utilization efficiency. Therefore, finding a balance between increasing the single-atom loading and maintaining a high level of atomic efficiency is a key research priority; 2) generally, the reliable bonds between the metal atoms and the carbon material substrate significantly optimize the distribution of the atomic electron cloud at the central active site, which in turn has the decisive modification on the electrocatalytic performance and durability of the nanomaterials. Obviously, our knowledge of such single-atom catalysts is still limited, such as what types of bonds the single metal atom forms with the substrate carbon material and what definite effects the introduced N atom has on the single metal atom catalytic performance and chemical activity centre. Therefore, a representative single metal-atom catalyst model with carbon material as the substrate, doped by the N atom, should be designed to investigate specifically and scientifically the close connection between the N atom and the central metal atom and the mechanism affecting the catalytic performance.

Therefore, we exploited a hard template and further heat treatment route to anchor single atom Co on nitrogen-rich carbon nanobox (Co@CNB-N_4) as an inexpensive and promising bifunctional catalyst in the field of overall water splitting. Polymerisation of polyvinyl pyrrolidone (PVP) on the surface of the metal oxide template and later passage of nitrogen gas provide rich sources of carbon and nitrogen for the single atom Co. At the same time, the high-temperature calcination led to the formation of a series of new bonds between Co and non-metallic elements, endowing significant increase in the loading and stability of Co atoms on the carbon nanobox. In particular, the uniformly dispersed single metal atoms and the designed regular nanobox structure would provide sufficient reaction centres for the overall water splitting,

promoting the electron transfer of OER/HER-related transition state species, and significantly boosting the activities. Furthermore, from the results of characterization and theoretical calculation, XAFS and DFT, the single-metal catalyst prepared by the template and heat treatment method exhibit the same coordination mode of nitrogen binding with the substrate material, which is Co@CNB-N_4 . Interestingly, the introduction of different transition metal elements resulted in different types of nitrogen in the carbon materials (pyridine, pyrrolic, and graphite), which affect electrocatalytic performance in different degrees. While metal Co rivets on the carbon material promoted the generation of pyrro-N, therefore Co@CNB-N_4 exhibits outstanding electrocatalytic performance in the field of overall water splitting, whose overpotential of HER was only 45 mV, close to benchmark Pt/C catalyst. For OER, Co@CNB-N_4 also possesses better catalytic performance than commercial RuO_2 catalyst, with an overpotential of 250 mV. And in a weak alkaline medium, as-prepared Co@CNB-N_4 keeps high stability for overall water splitting (100 h, close to 100 %) as well. This work devises completely a new and general strategy for the design of SACs by N-doped in the field of overall water splitting.

2. Experimental section

2.1. Materials

Iron(III) chloride (FeCl_3 , 98 %), Cobalt(II) nitrate hexahydrate ($\text{Co}(\text{NO}_3)_2 \cdot 6\text{H}_2\text{O}$, 99 %), ACETONE ($\text{C}_3\text{H}_6\text{O}$, 99.5 %) and Potassium Hydroxide (KOH , 99.99 %) were supplied from Adamas. Sodium Hydroxide (NaOH , ≥98 %), Ethanol ($\text{C}_2\text{H}_5\text{OH}$, ≥99.7 %) and deionized water (18.2 MΩ) were purchased from Greagent. Polyvinylpyrrolidone (PVP) was purchased from Sigma-Aldrich. Oxalic Acid ($\text{C}_2\text{H}_2\text{O}_4$, 97 %) was supplied from LeYan. All chemical reagents were used without any further purification.

2.2. The synthesis of electrocatalysts

2.2.1. The synthesis of Fe_2O_3 nanoboxes

The Fe_2O_3 nanoboxes were synthesized by a facile hydrothermal method. Typically, the same amount of 5.4 M NaOH solution and 2.0 M FeCl_3 solution were mixed evenly at 75 °C and formed colloids. Later, the gel was kept in a Teflon-lined stainless steel autoclave for 4 days at 100 °C. Finally, the reddish-brown product was washed four times with deionized water and ethanol, respectively, and dried in a vacuum of 70 °C for 8 h.

2.2.2. The synthesis of $\text{Fe}_2\text{O}_3/\text{PVP}$ nanoboxes

100 mg Fe_2O_3 nanoboxes were evenly dispersed in 100 mL solvent (ethanol: water = 1:4). Then, 100 mg PVP was added and treated with ultrasound until the uniform dark red solution was formed. The product was washed with deionized water and ethanol 4 times and dried in a vacuum of 70 °C for 8 h.

2.2.3. The synthesis of Co@CNB-N_4

100 mg of $\text{Fe}_2\text{O}_3/\text{PVP}$ nanoboxes and 80 mg of $\text{Co}(\text{NO}_3)_2 \cdot 6\text{H}_2\text{O}$ were first added into 100 mL of DI water and after 1 h continuous stirring, the mixed solution was transferred to Teflon-lined stainless steel autoclaved kettle and kept at 180 °C for 6 h. The product was washed with deionized water and ethanol 4 times and dried in a vacuum of 70 °C for 8 h to achieve $\text{Co@Fe}_2\text{O}_3/\text{PVP}$ nanoboxes. Then, the $\text{Co@Fe}_2\text{O}_3/\text{PVP}$ nanoboxes were annealed at 120 °C for 2 h and then annealed at 500 °C for 2 h under N_2 flow with a heating rate of 5 °C min⁻¹ to achieve $\text{Co@Fe}_2\text{O}_3/\text{PVP-N}_4$ nanoboxes. Afterward, the prepared sample was rapidly stirred with 0.5 M oxalic acid solution at 70 °C in order to remove the internal template. Finally, the product of Co@CNB-N_4 was washed with deionized water and ethanol for 4 times, and dried in a vacuum of 70 °C for 8 h. In control experiments, the single atom Co-anchored on carbon nanobox sample (Co@CNB) was prepared by a similar method, except

annealing under Ar flow. N-rich nanobox sample (CNB-N₄) was prepared by a similar method except for the introduction of Co atoms.

2.3. Material characterizations

The microsurface morphology were examined by ZEISS Gemini 300 (SEM) and FEI TF20 (TEM). Crystal characteristics, chemical bonds and functional groups are collected by Bruker D8 Advance (XRD), HORIBA Scientific LabRAM HR Evolution Raman spectrometer (Raman) and Thermo Scientific K-Alpha X-ray photoelectron spectrometer (XPS), respectively. The elemental analyses and specific surface area analysis were collected on an Inductively Coupled Plasma Optical Emission Spectrometry (ICP-OES) and Quantachrome Autosorb IQ3 instrument (BET). Accurate valence information can be obtained through 1W1B station in Shanghai Radiation (XAFS).

2.4. Electrochemical measurement

Classically, we use the CHI 760E electrochemical workstation to test a series of electrochemical experiments. Ni foam, Hg/HgO and graphite rod were used as working electrode, reference electrode and counter electrode, respectively. In order to test the performance of the catalyst at different pH values, 0.1 M KOH and 0.5 M H₂SO₄ were used as reaction media respectively. The ink contained 2 mg catalyst and was further dispersed evenly in a mixed solution (25 μL 5 wt% Nafion, 1 mL DI water). In this work, iR compensation (80 %) was used to correct the experimental results. Before the official test (sweep rate of 5.0 mV s⁻¹), CV cycles were usually performed. EIS tests were performed in a wide frequency range (100.0 kHz ~ 0.1 Hz). According to the convention, we standardized the experimental potential into reversible hydrogen potential (RHE), according to the formula:

$$E_{\text{RHE}} = E_{\text{Hg/HgO}} + 0.098 + 0.059\text{pH}$$

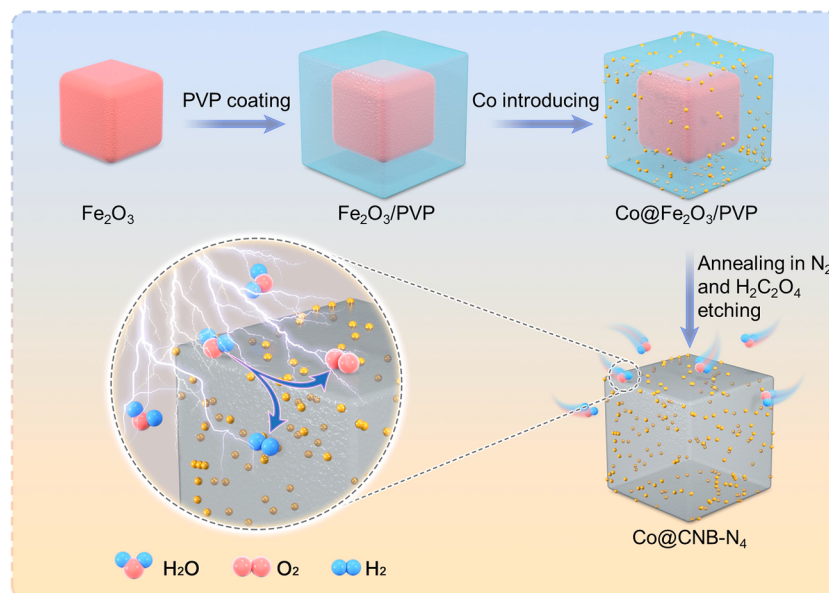
3. Results

3.1. Synthesis and characterization of Co@CNB-N₄ catalyst

The preparation process of Co@CNB-N₄ electrocatalyst is shown in Scheme 1. Briefly, homogeneous metal oxide cube template was synthesized firstly by a classical hydrothermal method, then coated with PVP and calcined in N₂ atmosphere to form carbon-based nanoboxes,

and finally the Fe₂O₃ core was removed by acid solution (see supporting information for the detailed description). Scanning electron microscopy (SEM) was used to observe the microstructures of Co@CNB-N₄, Co@CNB and CNB-N₄. Apparently, it's easy to find from Fig. 1a and Fig. S1 that all of the samples exist regular nanobox structures with uniform size and shape, benefiting from Fe₂O₃ nanoboxes as a template. The microscopic specific surface area and porosity of the as-prepared samples synthesized above were characterized by the nitrogen adsorption-desorption method, which is well known as an important index to affect the catalytic potential of the obtained catalysts. From the results of Brunauer-Emmett-Teller (BET) characterization (Fig. S2a), Co@CNB-N₄ exhibits the largest specific surface area (78 m²/g), which is slightly larger than those of Co@CNB (70 m²/g), CNB-N₄ (67 m²/g), respectively. It is worth noting that the three as-prepared samples have similar specific surface areas, due to their similar microstructures found by SEM analysis. The pore sizes of these samples are shown in Fig. S2b, and we can clearly observe that due to the nanobox structures with similar sizes, Co@CNB-N₄, Co@CNB, and CNB-N₄ have similar average pore diameters, which are 2.9, 2.8 and 2.6 nm, respectively, indicating these catalysts possess mesoporous structures. These results indicate that Co@CNB-N₄ possesses enough microscopic specific surface area and mesoporous nanostructure to contribute sufficiently abundant reactive centres and mass transport channels to actively boost the diffusion and permeation of various transition species during the catalytic process.

The microphysical nanostructure of Co@CNB-N₄ was further explored by Transmission electron microscopy (TEM) and high-resolution TEM (HRTEM) images, demonstrating that Co@CNB-N₄ does has a homogeneous nanobox structure (the thickness of Co@CNB-N₄ is about ~ 73 nm) to facilitate both charge transfer and catalytic processes (Fig. 1d). Notably, the high-resolution TEM (HRTEM) image (Fig. 1e) presents the highly ordered fringes of graphitic carbon and the pattern of ring-like selected area electron diffraction insert Fig. 1e also displays the good crystallinity of graphitic carbon. Importantly, it should be pointed out that there were no nanoparticles and nanoclusters being found in the carbon nanoboxes from the HAADF-STEM image of Co@CNB-N₄ (Fig. 1f). The uniform distribution of C, N and Co elements on the carbon nanoboxes could be intuitively displayed by Energy-dispersive X-ray spectroscopy (EDX) surface mapping scanning (Fig. 1g). Moreover, the content of Co element in Co@CNB-N₄ was detected by the coupled plasma optical emission spectrometry (ICP-OES) characterization to be 10.2 %, much higher than the previous



Scheme 1. Schematic illustration of synthesis of Co@CNB-N₄. The synthesis process of Co single atoms anchored on carbon nanoboxes.

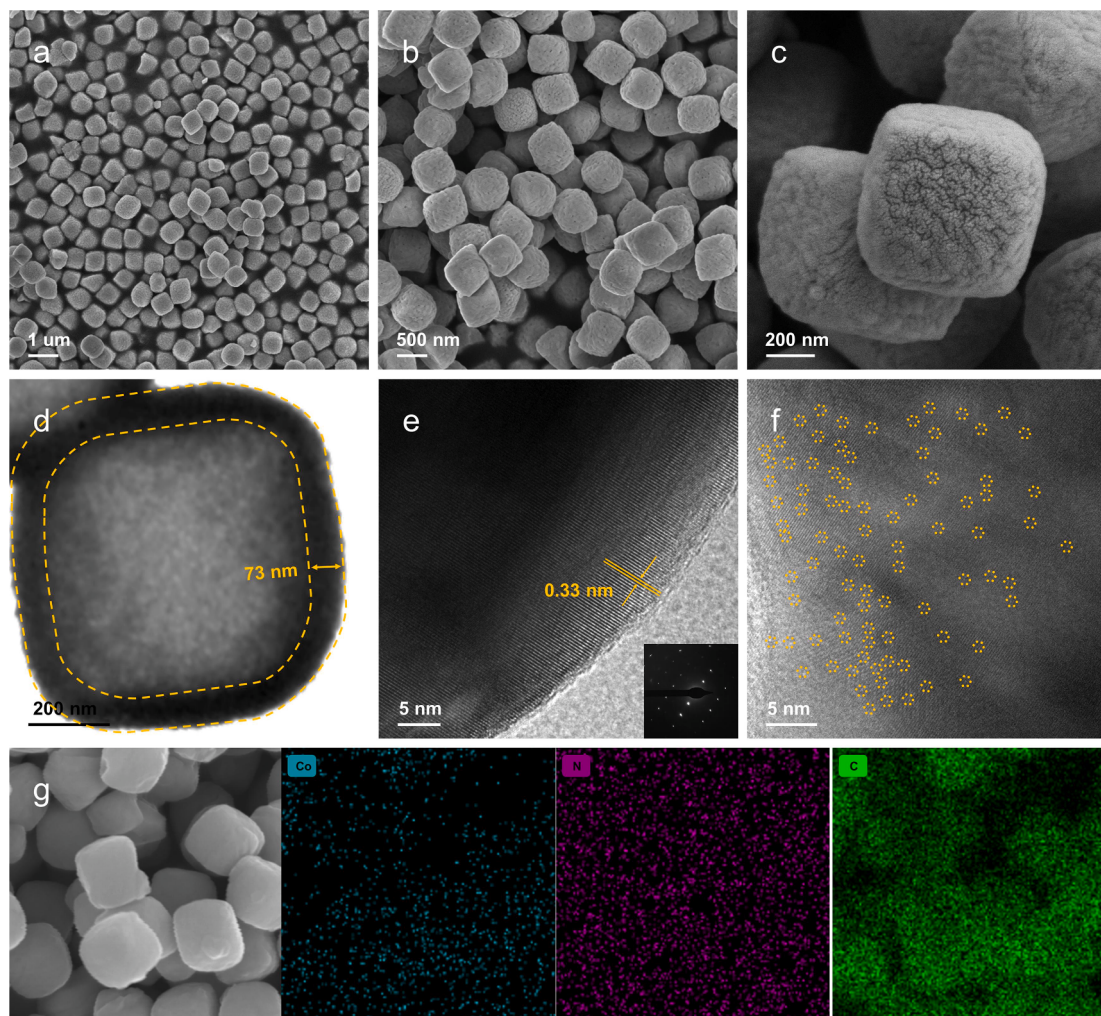


Fig. 1. Electron microscopy characterizations of Co@CNB-N₄. a–c FESEM images. d Low-magnification TEM image. e HRTEM image. Inset: the selected area electron diffraction spectrum (SAED) image. f Aberration-corrected HAADF-STEM image. Some bright dots are marked by orange circles. g The selected area and EDX surface elemental mapping images. (For interpretation of the references to colour in this figure legend, the reader is referred to the web version of this article.)

reports. The main reason is that PVP polymerizes to form reliable carbon substrates, and through further heat treatment, metal Co atoms are dispersed on the carbon nanoboxes materials to form a uniform texture single-atom catalyst. The above evidence indicates that homogeneous Co atoms are not only present on the surface of the carbon nanobox, but also embedded inside the carbon nanobox.

Besides, the X-ray diffraction (XRD, Fig. 2a) pattern of the as-prepared Co@CNB-N₄ displays similar diffraction centres with that of Co@CNB and CNB-N₄, two distinct diffraction peaks for graphitic

carbon are located at 28.2° (002) and 44.9° (001), respectively. Remarkably, no characteristic signal of Co element or Co compounds was detected in the crystallinity characterization, which further proved that the Co exists as the state of uniformly dispersed atoms in the as-prepared Co@CNB-N₄ sample, which is highly consistent with the TEM characterization. Furthermore, the bonding status of the fabricated samples was verified by Raman spectroscopy (Fig. 2b). Overall, only two characteristic signals were detected, attributed to the G band ($\sim 1585\text{ cm}^{-1}$) and the D band ($\sim 1327\text{ cm}^{-1}$), respectively. As we all know that

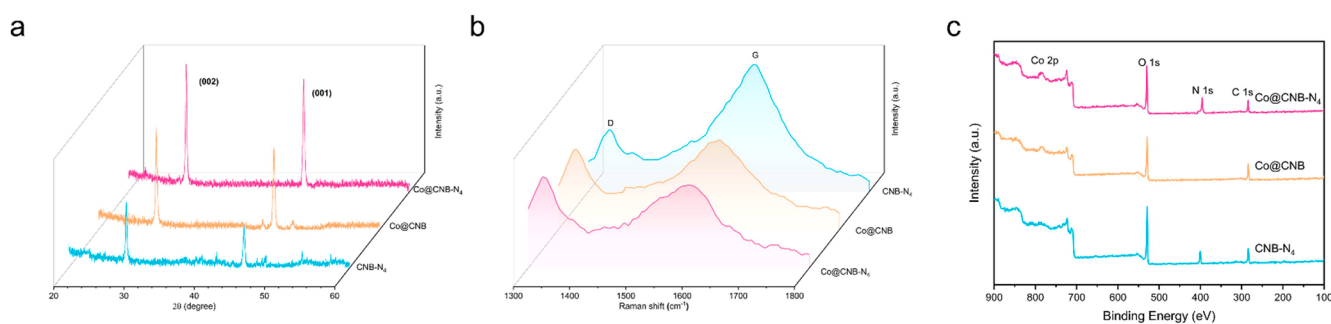


Fig. 2. Crystalline structural and chemical composition characterization. a XRD patterns, b Raman analysis and c XPS survey spectra of Co@CNB-N₄, Co@CNB, and CNB-N₄.

G band is attributed to sp^2 -hybridized, and the D band comes from sp^3 -hybridized and defects. In general, the higher the ratio of the D band to the G band (I_D/I_G), the more attractive defects of highly disordered carbon materials. Attractively, the I_D/I_G value of bare CNB-N₄ is only 0.49, while those of Co@CNB-N₄ and Co@CNB are 1.09 and 0.9, respectively, indicating that the introduction of single metal Co would make the carbon substrate tend to appear disordered phase structure, further improving the charge transfer rate, and improve the defect formation ability of carbon materials. Herein, more defective carbon structures result in larger surface areas and pore sizes.

The composition and chemical state of as-prepared catalysts were analyzed by X-ray photoelectron spectroscopy (XPS, Fig. 2c). The XPS spectrum of C 1s for Co@CNB-N₄ could be divided into three signals, located at ~284.5 eV, ~285 eV, ~285.7 eV and ~288.8 eV, attributing to C—C/C=C, C—N, C—O and Co-C bonds, respectively. Meanwhile, the C 1s spectrum of CNB-N₄ also shows similar sub-peaks, except Co@CNB-N₄ has no C—N bond centre. It is worth noting that the characteristic signal of the high-resolution Co 2p spectra (Fig. 3) shows that the state of Co species in the sample is only the oxidation state, not other states.

Moreover, the N 1s XPS spectra of Co@CNB-N₄ could present triple sub-centres, namely, pyridinic N (~398.3 eV), pyrrolic N (~400.1 eV) and graphitic N (~401.4 eV), respectively. Interestingly, compared to CNB-N₄, the characteristic peak position of pyrrolic N for Co@CNB-N₄ right-shifts by about 0.1 eV, and the content of pyrrolic N is the most (~85.1 wt%) among the three types of N in the high-resolution N 1s spectra of Co@CNB-N₄, which proves that Co is mainly bound to pyrrolic N in the substrate.

The coordination environment and the local structure between Co and non-metal atoms were analyzed at the atomic level by X-ray absorption spectroscopy tests. As displayed in Fig. 4a, the X-ray absorption near edge structure (XANES) spectra at Co K-edge reveals that the absorption edge of Co@CNB-N₄ is located between that of Co foil and Co₃O₄ and has a tendency to move to Co₃O₄, suggesting that the valence state of Co element in Co@CNB-N₄ close to +2/+3. Furthermore, it could be observed from the Co K-edge $k^3\chi(k)$ oscillation curves of the samples that the Co@CNB-N₄ curve has a clear oscillation curve (Fig. 4b), which is different from that of Co foil and Co₃O₄, meaning its local coordination environment is much different. And the Fourier

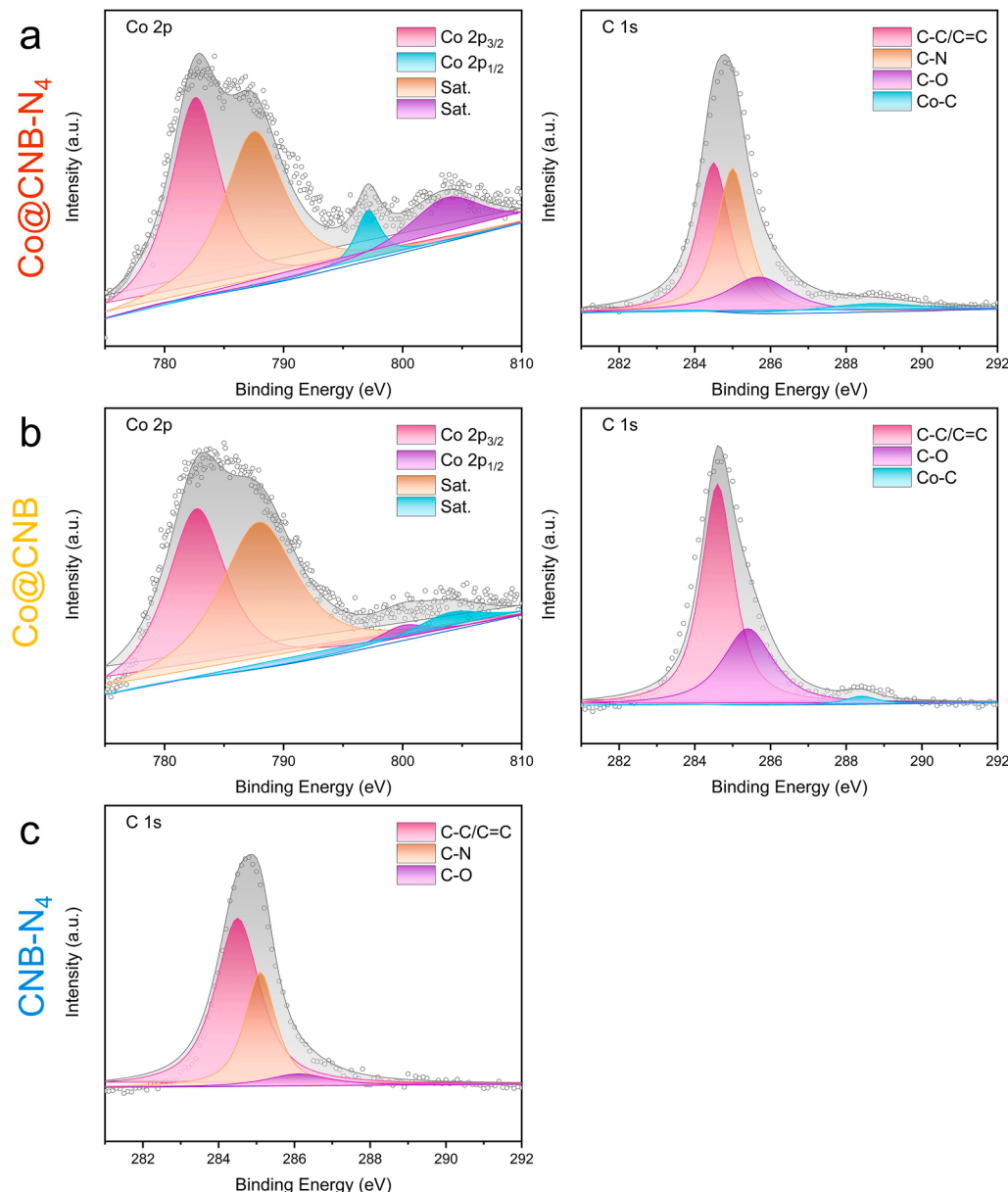
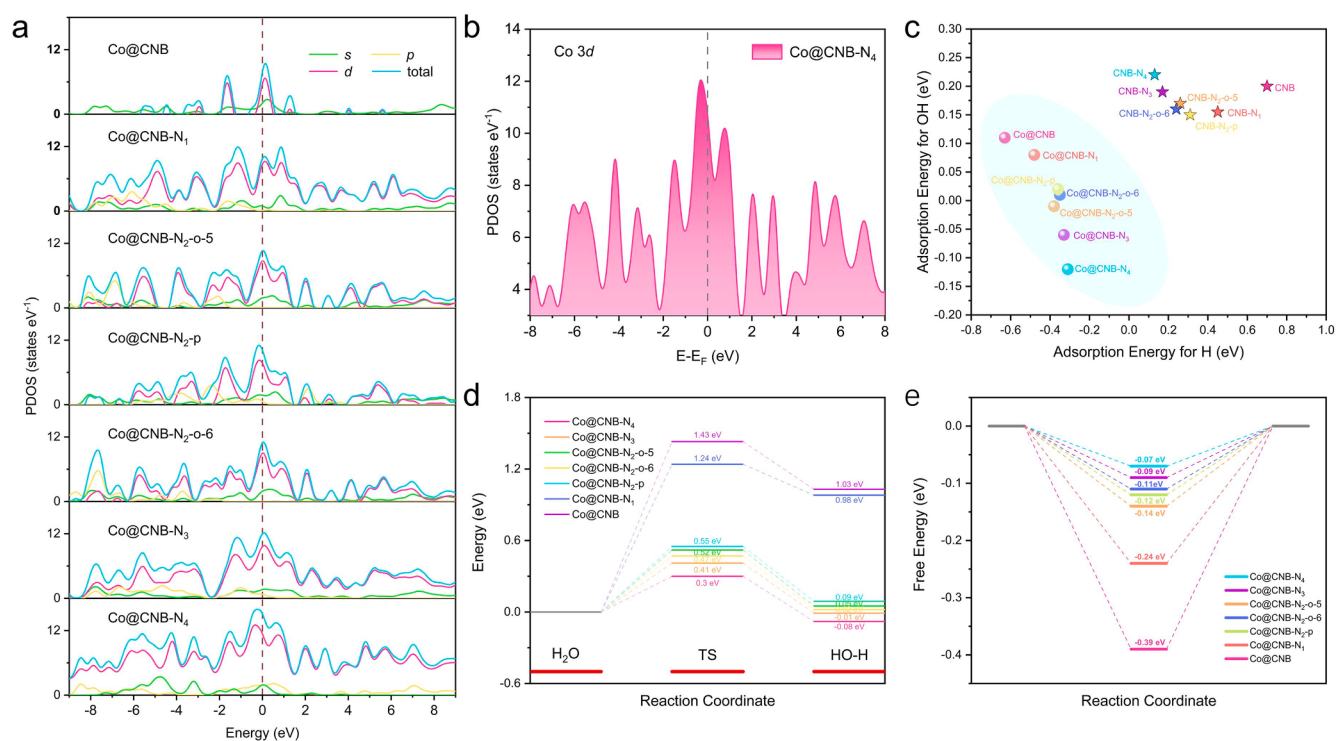
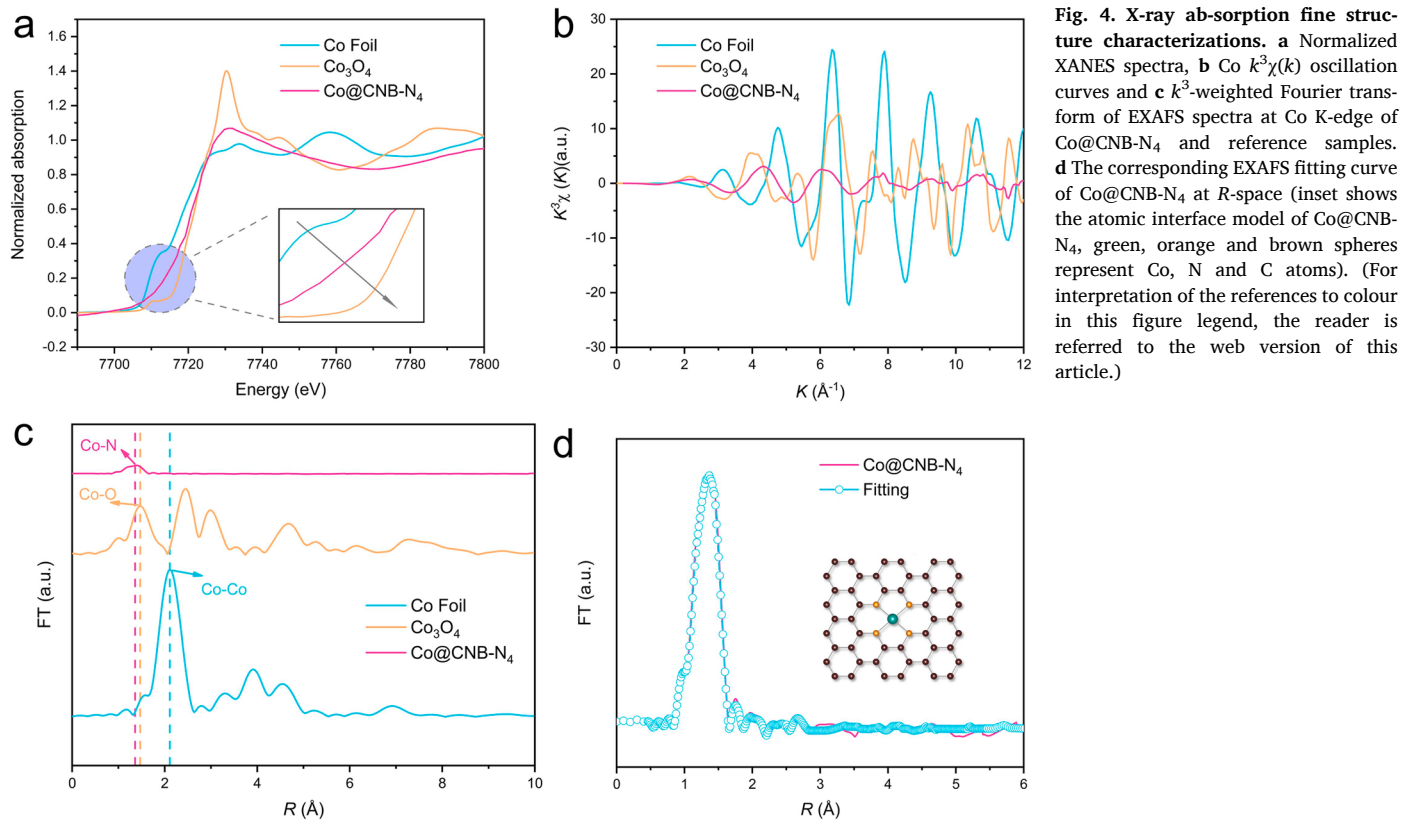


Fig. 3. High resolution chemical bond characterization. a The high resolution of Co 2p and C 1s of Co@CNB-N₄, **b** Co@CNB and **c** CNB-N₄, respectively.



transform (FT) curves in R space provide evidence for this striking distinction, showing only one prominent signal at 1.36 Å for Co@CNB-N₄, ascribing to Co-N first coordination shell. The characteristic signals of Co-Co (~2.11 Å), Co-O (~1.44 Å) and Co-C (~1.64 Å) have not been found intuitively, which fully proves that single-atom Co exists on nitrogen-rich carbon nanoboxes with reliable Co-N bonds (Fig. 4c). In order to extract the structural parameters of Co atom in Co@CNB-N₄ more accurately, the quantitative EXAFS curve was fitted by the ARTEMIS model (Fig. 4d). The fitting curves show that the central Co atom in Co@CNB-N₄ is coordinated by four N atoms, which are consisted by two pairs of similar bonds (five-membered and six-membered ring, 2:2), further confirming the single metal Co was successfully bonded on the substrate. To sum up, both the chemical characterization and microstructural analysis above of the materials demonstrate the successful synthesis of the *N*-doped single-metal Co catalyst with the coordination number of 4 for Co and N elements, which would be discussed in detail in the DFT calculation section below.

3.2. Theoretical investigations towards HER

Based on the above chemical and physical microstructure analysis, spin-polarized DFT calculations were performed to investigate the influences of the evolved coordinate configurations of the Co atom on the rational catalytic mechanism and intrinsic activity of the as-prepared Co@CNB-N_x catalysts. According to the different coordination environments of single metal Co atom, a series of models for Co@CNB-N_x ($x = 0, 1, 2, 3$ and 4) were shown in Fig. S13. The projected density of states (PDOS, Fig. 5a) of the Co@CNB-N_x indicates that Co@CNB-N₄ occupies higher density states than other models of Co@CNB-N_x near the Fermi level, suggesting electron transfer and conductivity of Co@CNB-N₄ is greatly boosted. Furthermore, by calculating the PDOS for a series of models, the results showed that the metal *d* orbitals make a major contribution to the DOS in Co@CNB-N_x. In particular, the *d* orbitals of all models which have Co species possess extremely high occupied states near the Fermi level, regardless of the number of N in the coordination environment. Furthermore, by comparing the *d* orbital features of the series of models (Fig. 5b), the results demonstrated that Co@CNB-N₄ possesses a wider 3*d* band and higher density than that of the other six models, implying that with the increase of the number of coordinating N, Co single metal could induce more free electrons. These findings are beneficial for H reactants adsorption, the activation of H₂O and the catalytic activity of the catalyst.

Moreover, we further investigated the reaction barrier of the modified catalysts in the field of overall water splitting in alkaline media. As is well known, the rate of the overall water splitting in the Volmer step depends mainly on what species or reaction centres are attached to the surface of the prepared catalysts by H and OH. Obviously, Fig. 5c reveals that all models with the introduction of Co single atoms exhibit better H and OH binding capacity compared to models without Co elements. And the level of H and OH adsorption by Co@CNB-N_x increases with the amount of coordinated N. More attractive, Co@CNB-N_x with four coordination N has the strongest water adsorption capacity (Fig. 5d) and the maximum value of release energy (~0.08 eV) for water dissociation in the Volmer step. And using the AB Initio Cluster-continuum Model, it is calculated that at the Co@CNB-N₄ interface, the dissociation of H₂O into H and OH requires reaction energy barriers of only 0.3 eV, demonstrating that the amount of N introduced makes a significant contribution to the dissociation of H₂O in alkaline media. The adsorption-free energy of H^{*}(ΔG_{H^*}) is often considered to be the most critical indicator for evaluating the catalytic activity of HER, while the ideal value of the adsorption-free energy is approximately zero. The value of ΔG_{H^*} for the Pt catalyst, the benchmark HER catalyst, is -0.09 eV. Therefore, we have calculated values of ΔG_{H^*} for seven models (Fig. 5e), clearly, the value of ΔG_{H^*} for Co@CNB-N₄ (~-0.07 eV) is lower than that of other models (Co@CNB-N₃, -0.09 eV; Co@CNB-N₂-o-6, -0.11 eV; Co@CNB-N₂-o-5, -0.14 eV; Co@CNB-N₂-p, -0.12 eV;

Co@CNB-N₁, -0.24 eV; Co@CNB, -0.39 eV). The above theoretical calculations and simulation tests provide further evidence that N doping could optimise the electronic environment of the central single metal and thus facilitate the HER catalytic process. Most importantly, the higher content of the pyrr-N, the more significant the improvement in HER performance, which would be discussed in more detail in the HER experiments section below.

3.3. Electrochemical performance toward HER

Based on the above chemical composition, microstructure and theoretical computations, the four N coordination Co@CNB-N₄ has the best HER catalytic in alkaline media among the as-prepared samples. Hence, the HER catalytic activity of a series of prepared catalysts (Co@CNB-N₄, Co@CNB, CNB-N₄) was tested in alkaline electrolytes (0.1 M KOH), including the noble metal catalyst (Pt/C, 20 wt%). As shown in Fig. 6a, the Co@CNB-N₄ displays better HER catalytic activity than that of other as-prepared samples, requiring only 45 mV, 85 mV and 163 mV to drive current densities of 10, 20 and 50 mA cm⁻², respectively. Even compared to the benchmark catalyst Pt/C, Co@CNB-N₄ also exhibits very close HER catalytic performance. Notably, the lower HER catalytic activity of CNB-N₄ without Co species introduction is mainly attributed to the limited active sites exposed by the aggregated materials, further illustrating the important role of dispersed single atoms Co as the active centre in the HER catalytic process. In addition, we derived the Tafel slopes from the LSV curves to validate the reaction kinetic properties of the as-prepared catalysts. Obviously, the Tafel slope of Co@CNB-N₄ was computed as ~ 117.5 mV dec⁻¹, which is much superior to that of Co@CNB (~205 mV dec⁻¹) and CNB-N₄ (~302.5 mV dec⁻¹), demonstrating that water dissociation (Volmer step) rather than hydrogen desorption (Heyrovsky step) is the rate-determining step in the HER reaction for this electrocatalyst under alkaline media (Fig. 6c). Besides, the value of charge transfer resistance (R_{ct}) for Co@CNB-N₄ (~6.04 Ω), as shown in Fig. 6d, is the smaller than that of Co@CNB (~9.66 Ω) and CNB-N₄ (~19.62 Ω) catalysts, which is mainly due to the enhanced electronic structure caused by the introduction of Co atoms and N elements, increasing the charge transfer capacity and conductivity during HER process.

Without good electrochemical stability, no large-scale application is possible, therefore long-term stability is an important indicator for evaluating electrocatalysts. The outstanding stability of Co@CNB-N₄ was tested by multiple cyclic voltammetry (CV) and i-t in the alkaline electrolyte. As presented in Fig. 6e, the HER catalytic properties and current density losses are negligible after 5000 cycles and the HAADF-STEM images (Fig. S7) of the material are very consistent. Furthermore, the i-t curve (insert Fig. 6e) reveals that the current density remains close to 10 mA cm⁻² after 50 h of driving at -0.085 V vsRHE, with only ~ 0.7 % change in Co atom content. And all the above results demonstrate the excellent electrochemical stability of the sample, which could be ascribed to the special bonding between the Co species and *N*-doped carbon nanosubstrates.

To further investigate the electrochemical surface area (ECSA) and the number of active sites of Co@CNB-N₄, we measured a series of CV curves at different sweep rates, fitting the current difference (Δj) at $E = 0.07$ V vs RHE linearly, and the slope of the fitted curve is the required double-layer capacitance (C_{dl}). The C_{dl} and the ECSA area are linearly related, so the ECSA of the samples could be obtained by a simple calculation. Not surprisingly, Co@CNB-N₄ demonstrated the largest capacitance (~175 mF) compared to the other as-prepared samples, which is in line with the conclusion of the specific surface area above, suggesting a correlation between electrochemical surface area and specific surface area. The ECSA was further calculated for each sample, obviously, Co@CNB-N₄ still has the larger ECSA value (~4375 cm²), while the ECSA values for Co@CNB and CNB-N₄ are only 2887.5 and 175 cm² respectively, further supporting the findings above. Additionally, the turnover frequencies (TOFs) of catalysts at the overpotentials of

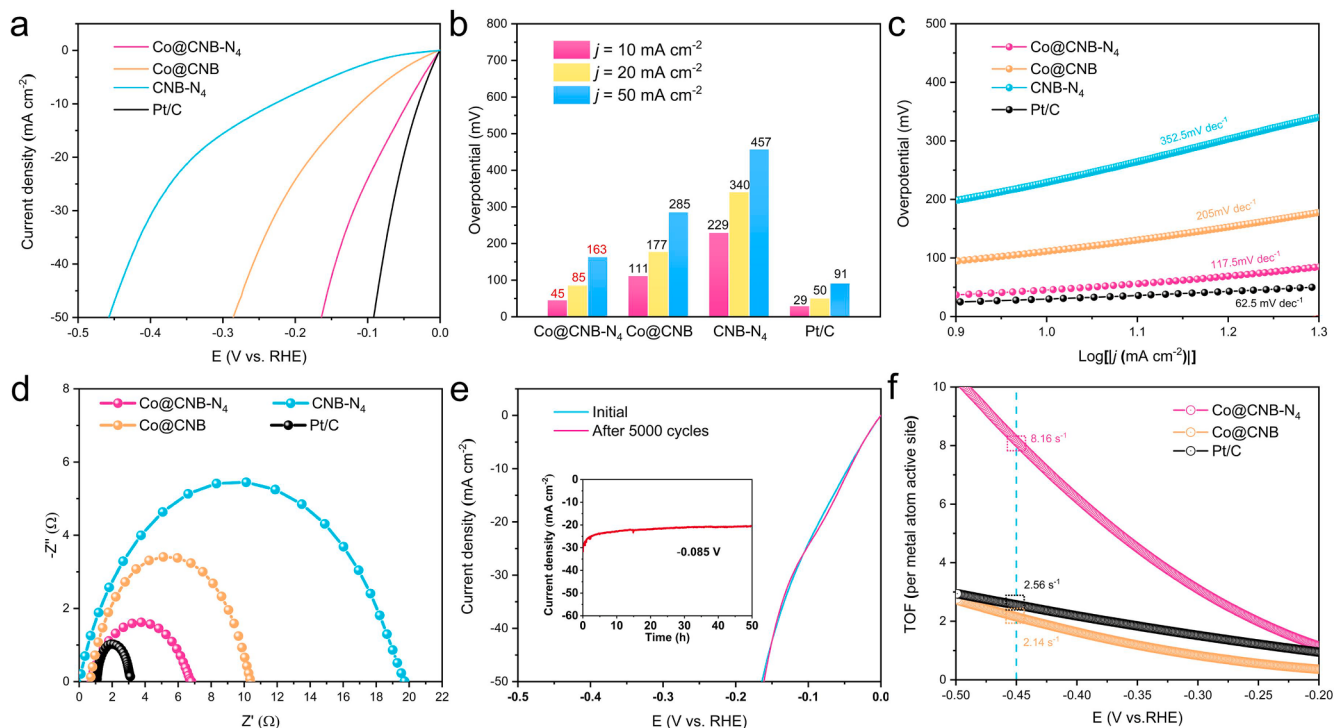


Fig. 6. Electrocatalytic alkaline HER performances of the catalysts in 0.1 M KOH electrolyte. a HER polarization curves of Co@CNB-N₄, Co@CNB, CNB-N₄ and Pt/C. **b** The comparison of overpotentials required to achieve 10, 20 and 50 mA cm⁻² for various catalysts. **c** Corresponding Tafel slopes originated from LSV curves. **d** EIS (Electrochemical Impedance Spectroscopy) Nyquist plots of the catalysts. **e** Stability test of Co@CNB-N₄ through cyclic potential scanning and chronoamperometry method (inset). **f** TOFs plots of the metal-based electrocatalysts.

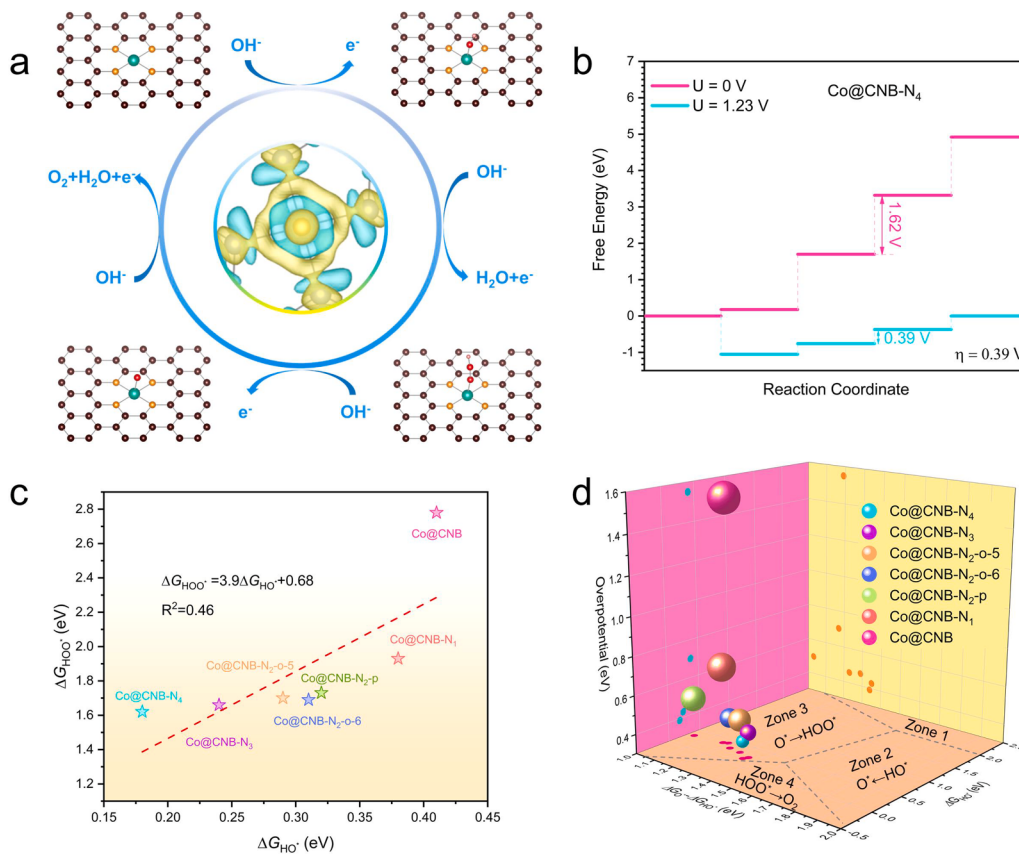


Fig. 7. DFT-calculated OER activities of Co@CNB-N_x. a Schematic diagram of the OER mechanism for Co@CNB-N₄ materials. The inset image is the localized electric-field distribution of Co@CNB-N₄. **b** Free-energy diagram of OER for Co@CNB-N₄. **c** Scaling relationship for Gibbs free energies of HOO* (ΔG_{HOO^*}) and HO* (ΔG_{HO^*}). **d** OER activity air bubble representing the overpotentials as a function of Gibbs free energies of the reaction intermediates. Z axis represents the value of OER overpotential. The grey dashed lines divide the bottom areas into four zones based on the potential-determining step.

450 mV were calculated (Fig. 6f), and the of Co@CNB-N₄ ($\sim 8.16 \text{ s}^{-1}$) is 3.81 and 3.18 times higher than that of Co@CNB ($\sim 2.14 \text{ s}^{-1}$) and Pt/C ($\sim 2.56 \text{ s}^{-1}$), respectively. Moreover, the exchange current density (j_0) is another significant index for assessing electrocatalytic performance, which is usually derived from Tafel plots after reasonable calculations. Again, Co@CNB-N₄ showed no disappointing value of j_0 ($\sim 0.0021 \text{ mA cm}^{-2}$), just lower than that of Pt/C ($j_0 = 0.0064 \text{ mA cm}^{-2}$) and far greater than that of the other two samples. The above phenomenon leads to the conclusion that uniform dispersion of single-atom catalysts with non-metallic elements as the coordination environment has a greater number of intrinsically active sites than the initial substrate.

3.4. Theoretical investigations towards OER

The mechanism of the HER reaction was explored above by DFT calculations. In order to further investigate the bonding pattern of the pyrr-N atom and the central Co single atom and the effect of the coordination number of pyrr-N on the electronic structure around the activation centre, the first principles density functional theory was therefore used to investigate the OER process based on the 4 e⁻ mechanisms proposed on a series of different Co@CNB-N_x (x = 0, 1, 2, 3 and 4) surfaces. The Co atom anchored on the carbon nanobox was selected as active site, and the 4e⁻ mechanism of the OER is given in Fig. 7a, along with the optimized structure of the four-step intermediate for Co@CNB-N₄. The substitution of a single Co atom for a C atom provides an abundance of free electrons for the coordinated pyrr-N element, a strategy that results in a higher valence state for the Co element and a lower valence state for the coordinated N element, which improves the adsorption of OH⁻ to the Co sites and H⁺ to the pyrr-N sites (supported by the difference in charge density distribution in Fig. 7a inset). This demonstrates that incorporating a single Co atom into the lattice of carbon could lead to redistribution of the electronic structure, resulting in an improved electronic environment for both HER and OER catalytic processes. For all the structures, each of the elementary steps is uphill and the OER rate-determining step is the conversion of the O^{*} group to the HOO^{*} group. Besides, by comparing Fig. 7b and S19, Co@CNB-N₄ presents the lowest overpotential of $\sim 390 \text{ mV}$, compared to Co@CNB-N₃ ($\sim 430 \text{ mV}$), Co@CNB-N₂-o-6 ($\sim 460 \text{ mV}$), Co@CNB-N₂-o-5 ($\sim 470 \text{ mV}$), Co@CNB-N₂-p ($\sim 500 \text{ mV}$), Co@CNB-N₁ ($\sim 700 \text{ mV}$) and Co@CNB ($\sim 1550 \text{ mV}$), suggesting that the abundant N in Co@CNB-N₄ provides sufficient lone electron pairs to incorporate Co atoms, thereby accelerating the OER reaction. And the limiting barrier of Co@CNB-N₄ is only 0.39 eV, while that of Co@CNB-N₃, Co@CNB-N₂-o-6, Co@CNB-N₂-o-5, Co@CNB-N₂-p, Co@CNB-N₁ and Co@CNB are 0.43 eV, 0.46 eV, 0.47 eV, 0.5 eV, 0.7 eV and 1.55 eV, respectively. Furthermore, ΔG_{HO}^* for Co@CNB-N₄ is 0.18 eV, indicating that the catalyst is not easily poisoned. Notably, when the number of coordination N is 2, Co@CNB-N₂ has three different configurations, including Co@CNB-N₂-o-6, Co@CNB-N₂-o-5 and Co@CNB-N₂-p. They possess extremely similar overpotentials, suggesting that there are many types of connections between Co and the substrate. This pattern could be also confirmed in the previous PDOS diagram (Fig. 5b), where Co@CNB-N₂-o-6, Co@CNB-N₂-o-5 and Co@CNB-N₂-p possess similar occupied states near the Fermi level, indicating that the conductivity and catalytic properties of the three configurations of Co@CNB-N₂ are closed. Therefore, the metal atoms and N elements in N-doped SACs have important impacts on improving catalytic activity, lowering the reaction barrier and further improving OER kinetics.

As displayed in Fig. 7c, we further assessed the limiting step and overpotentials using two factors, $\Delta G_{\text{O}}^* - \Delta G_{\text{HO}}^*$ and ΔG_{HO}^* . In a general sense, we used three descriptors, i.e., Gibbs free energy of adsorbed HOO^{*} (ΔG_{HOO}^*), O^{*} (ΔG_{O}^*) and HO^{*} (ΔG_{HO}^*), to evaluate the OER performance of catalysts. The various relationships between these transitional species are often used to describe the entire complex OER 4e⁻ process. Based on linear fitting ΔG_{HOO}^* and ΔG_{HO}^* , it is obtained that (Fig. 7c)

$$\Delta G_{\text{HOO}}^* = 3.9\Delta G_{\text{HO}}^* + 0.68$$

The bottom areas of the air bubble are divided into four zones based on the potential-determining step, which is the distribution of theoretical activity for Co@CNB-N_x (Fig. 7d).

The optimal Co@CNB-N_x model with the lowest overpotential and rate-limiting step could be clearly observed in the distribution diagram. Interestingly, the HO and catalyst interactions don't behave very strongly and the values of ΔG_{HO}^* are all positive, so zone 3 is the rate-determining step for all Co@CNB-N_x models, which is in line with above conclusion. Only theoretical calculations are not convincing and the following electrochemical tests were carried out on the OER performance of the samples.

3.5. Electrochemical performance toward OER

To visually evaluate the bifunctional electrocatalytic performance of Co@CNB-N₄, we subsequently measured the OER catalytic capacity of this catalyst in 0.1 M KOH alkaline electrolyte. As shown in Fig. 8a, Co@CNB-N₄ has outstanding OER catalytic potential with overpotentials of only 250 mV at the current density of 10 mA cm⁻², far lower than that of Co@CNB ($\sim 345 \text{ mV}$) and CNB-N₄ ($\sim 467 \text{ mV}$), and even superior to that of noble metal-based RuO₂ ($\sim 316 \text{ mV}$), which is superb in advanced transitional-metal-based OER electrocatalysts reported recently as well (Table S8, support information). Like HER, Co@CNB-N₄ also only requires overcoming the minimum energy barrier to drive current densities of 20 ($\sim 278 \text{ mV}$) and 50 ($\sim 328 \text{ mV}$) mA cm⁻², respectively, far lower than that of other samples, including RuO₂. At the same time, the slope of the corresponding Tafel fitted curve for Co@CNB-N₄ is 82.5 mV dec⁻¹, which is significantly smaller than that of Co@CNB ($\sim 162.5 \text{ mV dec}^{-1}$), CNB-N₄ ($\sim 165 \text{ mV dec}^{-1}$) and RuO₂ ($\sim 140 \text{ mV dec}^{-1}$), implying faster OER kinetics (Fig. 8b). This phenomenon could be attributed to the peculiar electronic environment around the Co single atom and the abundant pyrr-N content. As could be observed in Fig. S6, the Electrochemical impedance spectroscopy (EIS) Nyquist plots, the charge-transfer resistance (Rct) values for Co@CNB-N₄, Co@CNB, CNB-N₄ and RuO₂ are 7.31, 12.55, 17.98 and 9.99 Ω, respectively, confirming that N doping increases the kinetics of the OER, in line with recent findings on N-doped carbon nanomaterials. In order to assess the intrinsic activity of Co@CNB-N₄ in the OER process, TOF values representing the catalytic activity of each active site were derived (Fig. 8d), assuming that all metal atoms are involved in the catalysis and one metal atom contributes to one active site. And the TOF values at different overpotentials strongly demonstrate that Co@CNB-N₄ is one of the most active OER catalysts with the highest atom utilization efficiency. Moreover, we used long-term cyclic voltammetry (CV) and i-t tests to determine durability. And all results demonstrate that Co@CNB-N₄ has satisfactory electrochemical and structural stability, including mapping results after a long-term cycle (Fig. S9).

3.6. Electrochemical performance toward overall water splitting

Encouraged by the surprising catalytic activity of Co@CMB-N₄ for HER and OER, we have assembled a two electrodes system for overall water splitting. A two electrodes system consisting of Co@CNB-N₄ drives a current density of 10 mA cm⁻² at 1.59 V (Fig. 8e), which is 0.151, 0.388, and 0.095 V lower than that of Co@CNB || Co@CNB, CNB-N₄ || CNB-N₄, and RuO₂ || Pt/C, respectively. In addition, there was no particularly significant performance degradation in the long-term stability test with 100 h overall water splitting at different current densities (10, 50, and 100 mA cm⁻²) (Fig. S21), and no especially noticeable changes in microstructure were observed in the comparative SEM images of Co@CNB-N₄ (Fig. 8e). In particular, based on the measurement of the volumes of H₂ and O₂ prepared by the drainage method, the Faraday efficiency of 97 % was calculated for a two electrodes system

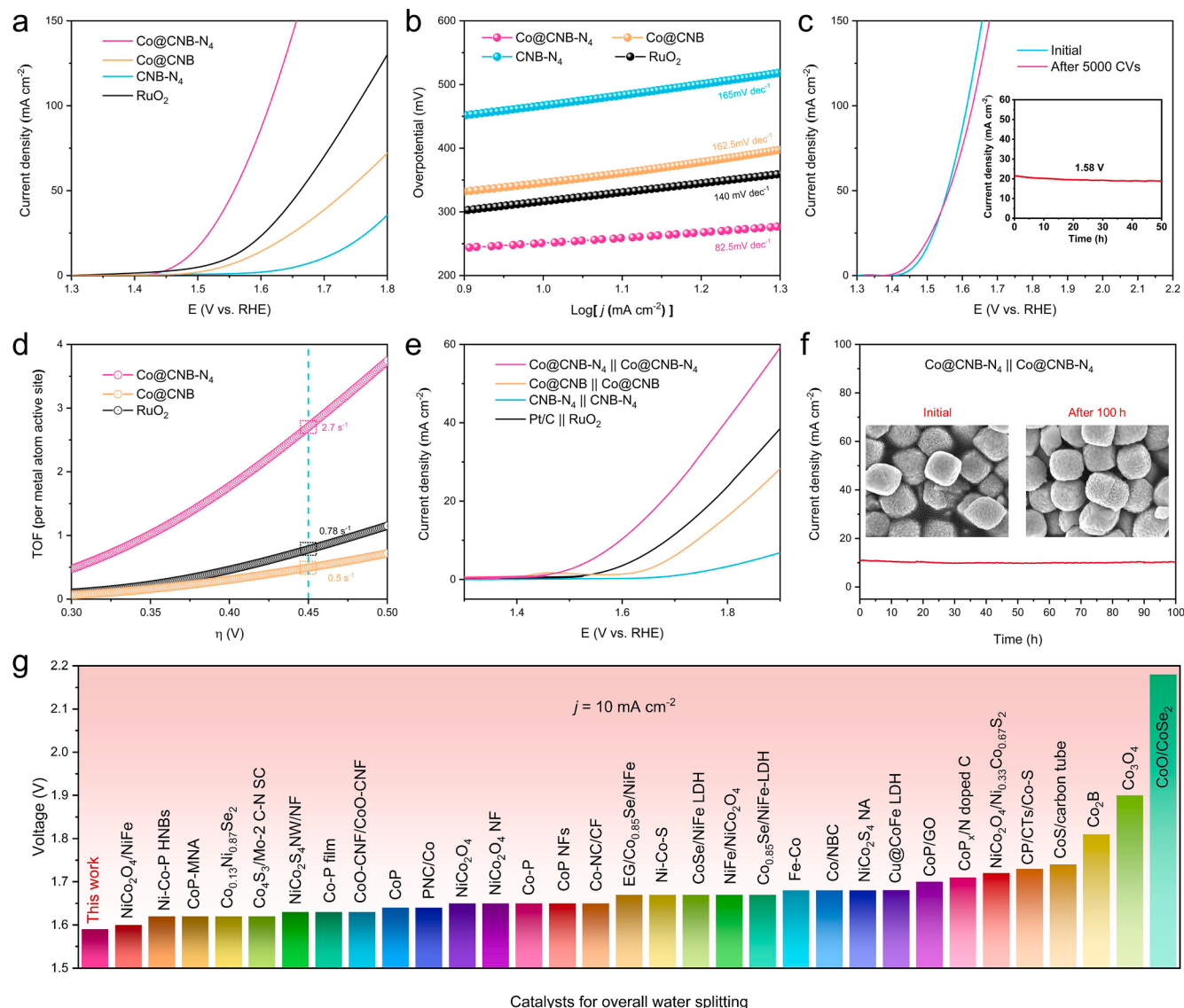


Fig. 8. Electrocatalytic alkaline OER and overall water splitting performances of the catalysts in 0.1 M KOH electrolyte. **a** LSV curves of Co@CNB-N_x and RuO₂ as OER electrocatalysts in 0.1 M KOH. **b** The corresponding Tafel plots. **c** LSV curves of Co@CNB-N₄ in 0.1 M KOH at the initial and after 5000 cycles and i-t curve (inset). **d** TOF values of different samples. **e** LSV polarization curves of as-prepared samples for overall water splitting. **f** Chronopotentiometry curve of the long-time stability of Co@CNB-N₄ for overall water splitting. The inset image shows the SEM comparison images before and after 100 h of stability. **g** Comparison of the overall water splitting activity for Co@CNB-N₄ with reported Co-based catalysts, originating from Table S9.

with Co@CNB-N₄ as double electrodes, which is very close to 100 %, i.e., the experimental and theoretical values remain in the high agreement.

4. Conclusion

In a word, we have developed a generic technology route with broad application prospects, including hard template method and further heat treatment to synthesize atomically uniformly dispersed Co riveted on N-rich morphologically and volumetrically uniform carbon nanoboxes. The reliable bondings between Co single metal and carbon nanoboxes provide extremely high metal loading on the as-prepared single-atom catalyst, resulting in satisfactory reactivity sites and excellent stability of Co@CNB-N₄. Based on XAFS characterization and STEM clear inspection, the best conformation of the Co-based single-atom catalyst in this work can be obtained as Co@CNB-N₄. Apparently, a series of Co@CNB-N_x models provide new approaches and new rationales for exploring and establishing more precisely the relationship between Co atoms or even single metal and N-enriched carbon-based substrates, and therefore can

be purposefully directed to improve HER and OER performance. Concretely, in this work, the presence of Co atoms directly promoted the formation of pyrr-N, therefore boosting the HER and OER processes, due to the fact that the best adsorption site for OH^{*} and H^{*} are Co and pyrr-N, respectively. Predictably, this work provides an effective scheme to successfully design single-atom catalysts with reasonable configurations for efficient HER and OER applications.

Declaration of Competing Interest

The authors declare that they have no known competing financial interests or personal relationships that could have appeared to influence the work reported in this paper.

Data availability

Data will be made available on request.

Acknowledgments

This work was partially sponsored by National Natural Science Foundation of China (52076126), Natural Science Foundation of Shanghai (18ZR1416200), Key Laboratory of Clean Power Generation and Environmental Protection Technology in Mechanical Industry. The authors would like to thank Shiyanjia Lab (www.shiyanjia.com) for the support of SEM, BET, and XPS test.

Appendix A. Supplementary data

Supplementary data to this article can be found online at <https://doi.org/10.1016/j.cej.2023.141435>.

References:

- [1] L.M. Wang, L.L. Zhang, W. Ma, H. Wan, X.J. Zhang, X. Zhang, S.Y. Jiang, J. Y. Zheng, Z. Zhou, In situ anchoring massive isolated Pt atoms at cationic vacancies of $\alpha\text{-Ni}_x\text{Fe}_{1-x}(\text{OH})_2$ to regulate the electronic structure for overall water splitting, *Adv. Funct. Mater.* 32 (2022) 2203342.
- [2] T. Li, X.X. Ma, J. Wu, F.H. Chu, L.X. Qiao, Y.B. Song, M.-L. Wu, J. Lin, L. Peng, Z. W. Chen, $\text{Ni}(\text{OH})_2$ microspheres in situ self-grown on ultra-thin layered g-C₃N₄ as a heterojunction electrocatalyst for oxygen evolution reaction, *Electrochim. Acta* 400 (2021), 139473.
- [3] T. Li, X.X. Ma, D.L. Wang, J. Wu, F.S. Zheng, J.W. Jin, Q.K. Wang, L.S. Hao, Z.J. Li, S.J. Huang, 3D Nanostructured nickel hydroxide as an efficient electrocatalyst for oxygen evolution reaction, *Electrocatalysis* 13 (2022) 873.
- [4] L. Hao, M. Zhou, Y. Song, X. Ma, J. Wu, Q. Zhu, Z. Fu, Y. Liu, G. Hou, T. Li, Tin-based perovskite solar cells: Further improve the performance of the electron transport layer-free structure by device simulation, *Sol. Energy* 230 (2021) 345.
- [5] T. Li, J. Wu, L.X. Qiao, Q.Z. Zhu, Z.G. Fu, J. Lin, J. Chen, L. Peng, B.F. Wang, Z. W. Chen, Bimetallic Ni-Hf tellurides as an advanced electrocatalyst for overall water splitting with layered g-C₃N₄ modification, *Mater. Today Energy* 26 (2022), 101002.
- [6] H. Wang, L. You, Y. Guan, H. Wang, X. Ma, D. Wang, J. Wu, Y. Zhu, J. Lin, J. Liu, Rational fabrication of flower-like VS₂-decorated Ti₃C₂ MXene heterojunction nanocomposites for supercapacitance performances, *Colloids Surf. A* 629 (2021), 127381.
- [7] J.J. Ge, J.Y. Zheng, J.W. Zhang, S.Y. Jiang, L.L. Zhang, H. Wan, L.M. Wang, W. Ma, Z. Zhou, R.Z. Ma, Controllable atomic defect engineering in layered $\text{Ni}_x\text{Fe}_{1-x}(\text{OH})_2$ nanosheets for electrochemical overall water splitting, *J. Mater. Chem. A* 9 (2021) 14432.
- [8] X.B. Zheng, J.R. Yang, Z.F. Xu, Q.S. Wang, J.B. Wu, E.H. Zhang, S.X. Dou, W.P. Sun, D.S. Wang, Y.D. Li, Ru-Co pair sites catalyst boosts the energetics for the oxygen evolution reaction, *Angew. Chem. Int. Ed.* 61 (2022) e202205946.
- [9] Z. Huang, J. Song, Y. Du, S. Xi, S. Dou, J.M.V. Nsanzimana, C. Wang, Z.J. Xu, X. Wang, Chemical and structural origin of lattice oxygen oxidation in Co-Zn oxyhydroxide oxygen evolution electrocatalysts, *Nat. Energy* 4 (2019) 329.
- [10] P. Zhu, X. Xiong, X.L. Wang, C.L. Ye, J.Z. Li, W.M.S.X.H. Sun, J.J. Jiang, Z. B. Zhuang, D.S. Wang, Y.D. Li, Regulating the FeN₄ moiety by constructing Fe-Mo dual-metal atom sites for efficient electrochemical oxygen reduction, *Nano Lett.* 22 (2022) 9507.
- [11] R.Z. Li, D.S. Wang, Understanding the structure-performance relationship of active sites at atomic scale, *Nano Res.* 15 (2022) 6888.
- [12] C. Roy, B. Sebok, S.B. Scott, E.M. Fiordaliso, J.E. Sensen, A. Bodin, D.B. Trimarco, C.D. Damsgaard, P.C.K. Vesborg, O. Hansen, I.E.L. Stephens, J. Kibsgaard, I. Chorkendorff, Impact of nanoparticle size and lattice oxygen on water oxidation on NiFeO_xH_y, *Nat. Catal.* 1 (2018) 820.
- [13] P. Zhu, X. Xiong, D.S. Wang, Regulations of active moiety in single atom catalysts for electrochemical hydrogen evolution reaction, *Nano Res.* 15 (2022) 5792.
- [14] Z.W. Seh, J. Kibsgaard, C.F. Dickens, I.B. Chorkendorff, J.K. Norskov, T. F. Jaraillo, Combining theory and experiment in electrocatalysis: Insights into materials design, *Science* 355 (2017) 4998.
- [15] S.L. Zhao, Y. Wang, J.C. Dong, C.T. He, H.J. Yin, P.F. An, K. Zhao, X.F. Zhang, C. Gao, L.J. Zhang, J.W. Lv, J.X. Wang, J.Q. Zhang, A.M. Khattak, N.A. Khan, Z. X. Wei, J. Zhang, S.Q. Liu, H.J. Zhao, Z.Y. Tang, Ultrathin metal-organic framework nanosheets for electrocatalytic oxygen evolution, *Nat. Energy* 1 (2016) 16184.
- [16] Y.Y. Liang, Y.G. Li, H.L. Wang, H.J. Dai, Strongly coupled inorganic/nanocarbon hybrid materials for advanced electrocatalysis, *J. Am. Chem. Soc.* 135 (2013) 2013.
- [17] C.C. McCrory, S. Jung, I.M. Ferrer, S.M. Chatman, J.C. Peters, T.F. Jaraillo, Benchmarking hydrogen evolving reaction and oxygen evolving reaction electrocatalysis for solar water splitting devices, *J. Am. Chem. Soc.* 137 (2015) 4347.
- [18] F. Dionigi, Z. Zeng, I. Sinev, T. Merzdorf, S. Deshpande, M.B. Lopez, S. Kunze, I. Zegkinoglou, H. Sarodnik, D. Fan, A. Bergmann, J. Drnec, J.F. de Araujo, M. Gliech, D. Teschner, J. Zhu, W.X. Li, J. Greeley, B.R. Cuanya, P. Strasser, In-situ structure and catalytic mechanism of NiFe and CoFe layered double hydroxides during oxygen evolution, *Nat. Commun.* 11 (2020) 2522.
- [19] Z.H. Zhang, D.H. Wu, X. Zhang, X.D. Zhao, H.C. Zhang, F. Ding, Z.J. Xie, Z. Zhou, First-principles computational studies on layered $\text{Na}_2\text{Mn}_3\text{O}_7$ as a high-rate cathode material for sodium ion batteries, *J. Mater. Chem. A* 25 (2017) 12752.
- [20] H.J. Cui, Z. Zhou, D.Z. Jia, Heteroatom-doped graphene as electrocatalysts for air cathodes, *Mater. Horiz.* 4 (2017) 7.
- [21] H. Wang, H.W. Lee, Y. Deng, Z. Lu, P.C. Hsu, Y. Liu, D. Lin, Y. Cui, Bifunctional non-noble metal oxide nanoparticle electrocatalysts through lithium-induced conversion for overall water splitting, *Nat. Commun.* 6 (2015) 7261.
- [22] Y.H. Wu, Y.Y. Yi, Z.T. Sun, H. Sun, T.Q. Guo, M.H. Zhang, L.F. Cui, K. Jiang, Y. Peng, J.Y. Sun, Bimetallic Fe-Ni phosphide carved nanoframes toward efficient overall water splitting and potassium-ion storage, *Chem. Eng. J.* 390 (2020), 124515.
- [23] H. Zhang, Y. Liu, T. Chen, J. Zhang, X.W. Lou, Unveiling the activity origin of electrocatalytic oxygen evolution over isolated Ni atoms supported on a N-doped carbon matrix, *Adv. Mater.* 31 (2019) 1904548.
- [24] T. Wang, G. Nam, Y. Jin, X. Wang, P. Ren, M.G. Kim, J. Liang, X. Wen, H. Jang, J. Han, Y. Huang, Q. Li, J. Cho, NiFe(O_x) hydroxides derived from NiFe sulfides as an efficient oxygen evolution catalyst or rechargeable Zn-air batteries: the effect of surface S residues, *Adv. Mater.* 30 (2018) 1800757.
- [25] X. Xu, F. Song, X. Hu, A nickel iron diselenide-derived efficient oxygen-evolution catalyst, *Nat. Commun.* 7 (2016) 12324.
- [26] J. Nai, Y. Lu, L. Yu, X. Wang, X.W. Lou, Formation of Ni-Fe mixed diselenide nanocages as a superior oxygen evolution electrocatalyst, *Adv. Mater.* 29 (2017) 1703870.
- [27] N.T. Suen, S.F. Hung, Q. Quan, N. Zhang, Y.J. Xu, Electrocatalysis for the oxygen evolution reaction: recent development and future perspectives, *Chen. Chem. Soc. Rev.* 46 (2017) 337.
- [28] G. Moon, M. Yu, C.K. Chan, H. Taysuz, Highly Active Cobalt-Based Electrocatalysis with Facile Incorporation of Dopants for the Oxygen Evolution Reaction, *Angew. Chem. Int. Ed.* 131 (2019) 3529.
- [29] J.X. Sun, P. Leng, Y.H. Xie, X.X. Yu, K.G. Qu, L.G. Feng, H.F. Bao, F. Luo, Z.H. Yang, Co single atoms and Co nanoparticle relay electrocatalyst for rechargeable zinc air batteries, *Appl. Catal. B Environ.* 319 (2022), 121905.
- [30] X. Li, S. Guo, W. Li, X. Ren, J. Su, Q. Song, A.J. Sobrido, B. Wei, Edge-rich MoS₂ grown on edge-oriented three-dimensional graphene glass for high-performance hydrogen evolution, *Nano Energy* 57 (2019) 388.
- [31] C. Zhu, Q. Shi, S. Feng, D. Du, Y. Lin, Single-atom catalysis for electrochemical water splitting, *ACS Energy Lett.* 3 (2018) 1713.
- [32] C. Tang, R. Zhang, W. Lu, L. He, X. Jiang, A.A. Asiri, X. Sun, A Mn-doped Ni₂P nanosheet array: an efficient and durable hydrogen evolution reaction electrocatalyst in alkaline media, *Adv. Mater.* 29 (2017) 1602441.
- [33] G. Moon, M. Yu, C.K. Chan, H. Taysuz, Highly Active Cobalt-Based Electrocatalysts with Facile Incorporation of Dopants for the Oxygen Evolution Reaction, *Angew. Chem. Int. Ed.* 131 (2019) 3529.
- [34] P. Zhang, H. Xiang, L. Tao, H. Dong, Y. Zhou, T.S. Hu, X. Chen, S. Liu, S. Wang, S. Garaj, Chemically activated Mo₂ for efficient hydrogen production, *Nano Energy* 57 (2019) 535.
- [35] L.X. Ge, M.H. Qiu, Y.F. Zhu, S. Yang, W.Q. Li, W.T. Li, Z. Jiang, X.Q. Chen, Synergistic catalysis of Ru single-atoms and zeolite boosts high-efficiency hydrogen storage, *Appl. Catal. B Environ.* 319 (2022), 121958.
- [36] C. Zhu, Q. Shi, S. Feng, D. Du, Y. Lin, Single-atom catalysts for electrochemical water splitting, *ACS Energy Lett.* 3 (2018) 1713.
- [37] B.T. Qiao, A.Q. Wang, X.F. Yang, L.F. Allard, Z. Jiang, Y.T. Cui, J.Y. Liu, J. Li, T. Zhang, Single-atom catalysis of CO oxidation using Pt/FeO_x, *Nat. Chem.* 3 (2011) 634.
- [38] J. Zhang, J. Liu, L. Xi, Y. Yu, N. Chen, S. Sun, W. Wang, K.M. Lange, B. Zhang, Single-atom Au/NiFe layered double hydroxide electrocatalyst: probing the origin of activity for oxygen evolution reaction, *J. Am. Chem. Soc.* 140 (2018) 3876.
- [39] Q. Cheng, L. Yang, L. Zou, Z. Zou, C. Chen, Z. Hu, H. Yang, Single cobalt atom and N codoped carbon nanofibers as highly durable electrocatalyst for oxygen reduction reaction, *ACS Catal.* 7 (2017) 6864.
- [40] C. Zhao, Y. Wang, Z. Li, W. Chen, Q. Xu, D. He, D. Xi, Q. Zhang, T. Yuan, Y. Qu, Solid-diffusion synthesis of single-atom catalysts directly from bulk metal for efficient CO₂ reduction, *Joule* 3 (2019) 584.
- [41] H. Fei, J. Dong, Y. Feng, C.S. Allen, C. Wan, I. Shakir, et al., General synthesis and definitive structural identification of MN₄C₄ single-atom catalysts with tunable electrocatalytic activities, *Nat. Catal.* 1 (2018) 63.
- [42] X. Gao, L. Yin, L. Zhang, Y. Zhao, B. Zhang, Decoration of NiCoP nanowires with interlayer-expanded few-layer MoSe₂ nanosheets: A novel electrode material for asymmetric supercapacitors, *Chem. Eng. J.* 395 (2020), 125058.
- [43] D.C. Nguyen, T.L.L. Doan, S. Prabhakaran, D.H. Kim, N.H. Kim, J.H. Lee, Rh single atoms/clusters confined in metal sulfide/oxide nanotubes as advanced multifunctional catalysts for green and energy-saving hydrogen productions, *Appl. Catal. B Environ.* 313 (2022), 121430.
- [44] N. Cheng, S. Stambula, D. Wang, M.N. Banis, J. Liu, A. Riese, B. Xiao, R. Li, T. K. Sham, L.M. Liu, G.A. Botton, X. Sun, Platinum single-atom and cluster catalysis of the hydrogen evolution reaction, *Nat. Commun.* 7 (2016) 13638.
- [45] Y. Peng, W. Pan, N. Wang, J.E. Lu, S. Chen, Ruthenium ion-complexed graphitic carbon nitride nanosheets supported on reduced graphene oxide as high-performance catalysts for electrochemical, *ChemSusChem* 11 (2018) 130.
- [46] S. Yao, X. Zhang, W. Zhou, R. Gao, W. Xu, Y. Ye, L. Lin, X. Wen, P. Liu, B. Chen, E. Crumlin, D. Ma, et al., Atomic-layered Au clusters on $\alpha\text{-MoC}$ as catalysts for the low-temperature water-gas shift reaction, *Science* 357 (2017) 389.
- [47] J. Liu, Catalysis by supported single metal atoms, *ACS Catal.* 7 (1) (2017) 34–59.
- [48] W. Chen, J. Pei, C.T. He, J. Wan, H. Ren, Y. Zhu, Y. Wang, J. Dong, S. Tian, W. C. Cheong, S. Lu, X. Zheng, W. Yan, A. Zhuang, C. Chen, Q. Peng, D. Wang, Y. Li,

- Rational design molybdenum atoms anchored on N-doped carbon for effective hydrogen evolution reaction, *Angew. Chem. Int. Ed.* 56 (2017) 16086.
- [49] J. Zhang, Y. Zhao, C. Chen, Y.C. Huang, C.L. Dong, C.J. Chen, R.S. Liu, C. Wang, K. Yan, Y. Li, G. Wang, Tuning the coordination environment in single-atom catalysis to achieve highly efficient oxygen reduction reactions, *J. Am. Chem. Soc.* 141 (2019) 20118.
- [50] H.W. Liang, S. Brüller, R. Dong, J. Zhang, X. Feng, K. Müllen, Molecular metal-N_x centres in porous carbon for electrocatalytic hydrogen evolution, *Nat. Commun.* 6 (2015) 7992.
- [51] D. Liu, S. Ding, C. Wu, W. Gan, C. Wang, D. Cao, Z.U. Rehman, Y. Sang, S. Chen, X. Zheng, Synergistic effect of an atomically dual-metal doped catalyst for highly efficient oxygen evolution, *J. Mater. Chem. A* 6 (2018) 6840.